ACS APPLIED MATERIALS & INTERFACES

Research Article

www.acsami.org

Au−Ag@Au Hollow Nanostructure with Enhanced Chemical Stability and Improved Photothermal Transduction Efficiency for Cancer Treatment

Tongtong Jiang,[†] Jiangluqi Song,[†] Wenting Zhang,[†] Hao Wang,[†] Xiaodong Li,[†] Ruixiang Xia,[*,‡] Lixin Zhu,[*,‡] and Xiaoliang Xu[*,†]

[†]Key Laboratory of Strongly-Coupled Quantum Matter Physics, Chinese Academy of Sciences, School of Physical Sciences, University of Science and Technology of China, No. 96 Jinzhai Road, Hefei, Anhui Province 230026, China

[‡]Center Laboratory, First Affiliated Hospital of Anhui Medical University, Hefei, Anhui Province 230026, China

Supporting Information

ABSTRACT: Despite the fact that Au−Ag hollow nanoparticles (HNPs) have gained much attention as ablation agents for photothermal therapy, the instability of the Ag element limits their applications. Herein, excess Au atoms were deposited on the surface of a Au−Ag HNP by improving the reduction power of L-ascorbic acid (AA) and thereby preventing the reaction between $HAuCl_4$ and the Ag element in the Au−Ag alloy nanostructure. Significantly, the obtained Au−Ag@Au HNPs show excellent chemical stability in an oxidative environment, together with remarkable increase in extinction peak intensity and obvious narrowing in peak width. Moreover, finite-difference time-domain (FDTD) was used to simulate the optical properties and electric field distribution of HNPs. The calculated results show that the proportion of absorption cross section in total extinction cross section increases with the improvement of Au content in HNP. As predicted by the theoretical calculation results, Au−Ag@Au nanocages (NCs) exhibit a photothermal transduction efficiency (η) as high as 36.5% at 808 nm, which is higher than that of Au−Ag NCs (31.2%). Irradiated by 808 nm laser at power densities of 1 W/cm^2, MCF-7 breast cancer cells incubated with PEGylated Au−Ag@Au NCs were seriously destroyed. Combined together, Au−Ag@Au HNPs with enhanced chemical stability and improved photothermal transduction efficiency show superior competitiveness as photothermal agents.

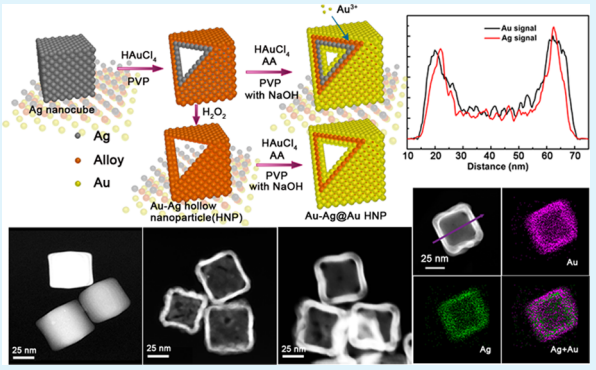

KEYWORDS: *alloy, photothermal therapy, absorption, hollow nanostructure, stability*

INTRODUCTION

Au nanoparticles (NPs) have attracted great attention as photothermal materials due to their distinctive properties including stability, low cytotoxicity, biocompatibility, tunable local surface plasmon resonances (LSPR) peak, and surface modification by a wide range of thiolated molecules.[1−7] Photothermal therapy is a noninvasive treatment, in which the absorbed energy of NPs can be efficiently enhanced, converting into heat sufficient to destroy cancer cell in the local vicinity of the particle by matching the SPR peak of NPs with the excitation light wavelength.[7−9] At a certain excitation frequency, the incident light couples to the plasma resonance of the conduction electron, resulting in a strong collective oscillation on the surface of the NP, namely, LSPR mode.[1,10−12] At LSPR mode, strong electromagnetic fields would be localized around the NP.[13] The far-field properties of metal NPs (such as absorption, scattering, and extinction) and its near-field properties (such as the intensity and spatial distribution of the electromagnetic field enhancements) are related to the size, shape, and morphology of the particle.[14,15] The extinction cross section is determined by the strength of both scattering (radiative) and absorptive (nonradiative) processes.[16,17] Absorption depends on volume (CA $\approx r^3$, where r is the particle radius), whereas scattering depends on volume squared (CS $\approx r^6$).[17] Photothermal therapy is usually conducted with an 808 nm laser, where the penetration depth of light in biological tissue is maximum owing to the relatively low absorption/scattering by hemoglobin and water in this so-called transparent window.[8,18,19]

Over the past decade, Au photothermal transducers with different morphologies (e.g., Au nanostar,[7] Au nanoshell,[8] Au nanorod,[17] and Au nanocage (NC)[20]) have been reported. The SPR peaks of these NPs can be efficiently tuned to the near-infrared (NIR) range of the spectrum (700−1100 nm). Of these photothermal transducers, Au NCs have the higher photothermal transduction efficiency per Au atom and special

Received: July 25, 2015
Accepted: September 14, 2015
Published: September 15, 2015

DOI: 10.1021/acsami.5b08305
ACS Appl. Mater. Interfaces 2015, 7, 21985−21994

hollow structure, serving as carriers for the delivery of payload.[18,21] Au NCs were synthesized by using Ag nanocubes as a sacrificial template through the galvanic replacement reaction.[20] Au NCs with SPR peaks extending into the NIR region still contain some Ag.[22] The Ag element limits their potential SPR-based application due to high susceptibility of Ag to oxidation under condition that involve oxidants, acid, water, and heating.[2,23] H_2O_2, an effective etching agent of the Ag element, is involved in many biological processes and enzymatic reactions related to intracellular oxidative stress and aging.[24] The Ag element in Au−Ag nanostructure[23,25] can be etched by H_2O_2 and is released in the form of Ag^+, which would induce shifting of the SPR peak, causing the reduction of absorbed energy and greater toxicity of Au−Ag NC.[18,24] It is necessary to improve the stability of Au−Ag NC against the etching of H_2O_2. Depositing a shell has been considered as an effective method.[4] Traditional SiO_2 shell is a common material for enhancing stability, improving biocompatibility, and preserving the plasmon resonance from an aggregation shift.[4,26] T. R. Lee and co-workers demonstrated that hollow gold−silver nanoshells within porous silica have enhanced colloidal stability.[27] However, small molecules and metal ions can penetrate through the porous silica shell. Whether dense silica shell can prevent the penetration of H_2O_2 needs to be determined. For the alloy NP, the stability depends on the Ag/Au ratio; corrosion easily starts from unstable domains upon exposure to an etchant.[28,29] The stability increases as the Ag content decreases.[29] Further galvanic replacement reaction and the etching of H_2O_2 can reduce the amount of Ag, but the SPR peak position of Au−Ag NCs would be red-shifted, causing the mismatching with laser wavelength, and the peak intensity would have obvious reduction, causing a significant decrease of the molar extinction coefficient.[22,24] Depositing Au atoms on the surface of Ag core (or Au−Ag alloy) is difficult due to the galvanic replacement reaction between Ag and $HAuCl_4$, even though Au and Ag have the close lattice match (<0.3% mismatch).[30] Most recently, Qin and co-workers demonstated a fast parallel reduction by AA to compete with and block the replacement reaction for the galvanic replacement-free deposition of Au on Ag nanocube having enhanced chemical stability and surface-enhanced Raman spectroscopy (SERS) activity.[31] Kitaev and co-workers proposed that slow addition of gold tetrachloroaurate together with citrate achieves uniform gold plating of silver decahedral NPs possessing enhanced chemical stability and plasmonic properties.[32] However, these research studies are largely devoted to coating Au shell around Ag NP for researching SERS activity or discussing the synthesis strategy of Au shell.[2,30,31] There are few studies about discussing the stability of Au−Ag alloy NCs and the strategy of improving their chemical stability for biological application.

By researching the penetration ability of etchants through SiO_2 shell, it was found that SiO_2 shell cannot well protect Au−Ag hollow nanoparticles (HNPs) in an oxidation environment (H_2O_2). Herein, Au atoms were deposited on the inner and outer surface of Au−Ag NC at a sufficiently high pH in the presence of $HAuCl_4$ and AA. With changing the amount of NaOH and $HAuCl_4$ added in the reaction solution, the SPR peak position of HNPs can be precisely controlled. The obtained Au−Ag@Au HNPs have much stronger extinction peak intensities, narrower bandwidths, and higher chemical stabilities against H_2O_2 etching. To deeply research LSPR properties of HNPs, FDTD solution was used to simulate the electric field distribution and calculate the extinction (absorption and scattering) cross section of HNPs. Au−Ag@Au NCs exhibit marked photoinduced heating and higher photothermal transduction efficiency than Au−Ag NCs. Photothermal treatment studies were demonstrated on MCF-7 breast cancer cells, which showed that Au−Ag@Au NCs are effective for the destruction of cancer cells.

EXPERIMENTAL METHODS

Materials. Poly(vinylpyrrolidone) (PVP, powder, MW ≈ 55 000) and sodium hydrosulfide (NaHS) were purchased from Sigma-Aldrich. Silver trifluoroacetate (CF_3COOAg) was purchased from Alfa Aesar. Hydrochloric acid (HCl, 36−38%, AR), hydrogen peroxide (H_2O_2, 30%, AR), ethanol (99.7%, AR), sodium chloride (NaCl, 99.0%), ammonia solution (NH_4OH, 25−28%, AR), acetone (99.5%, AR), ethylene glycol (EG, 99.0%, AR), tetraethyl orthosilicate (TEOS, 28.4%, AR), chloroauric acid ($HAuCl_4$), L-ascorbic acid (AA, 99.7%), and sodium hydroxide (NaOH, 96.0%) were purchased from Sinopharm Chemical Reagent Co., Ltd. mPEG-thiol (methoxypoly-(ethylene glycol)thiol, MW ≈ 5 000) was purchased from Laysan Bio, Inc. Cell culture media, supplements, and cancer cells were all supplied by First Affiliated Hospital of Anhui Medical University. All the chemicals were used without further purification. The water used had a resistivity higher than 18.25 MΩ·cm.

Synthesis of Ag Nanocube. Ag nanocubes were prepared according to the sulfide-mediated polyol method.[22] In the synthesis process, CF_3COOAg was used in the consideration of the reproducibility and relatively high quality of the product.[33] Typically, 10 mL of EG was added to a reaction vial and heated in an oil bath at 150 °C for 1 h. NaHS (120 μL; 3 mM in EG) was injected. After 2 min, 1 mL of HCl (3 mM in EG) was introduced, followed by adding 2.5 mL of PVP (20 mg/mL in EG). After another 2 min, 0.8 mL of CF_3COOAg (282 mM in EG) was added into the mixture. With reaction for different times, the vial was placed into ice water to suspend the reaction.

Preparation of Ag Nanocube@SiO_2. Ag@SiO_2 particles were prepared according to the modified Stöber method.[28] Forty mL of ethanol, 8 mL of water, 6 mL of Ag ethanol solution (4.7 mM), and 1 mL of ammonia were mixed together. TEOS ethanol solution (1% (v/v)) was added slowly. The reaction was kept for 12 h.

Synthesis of Au−Ag NC. Au−Ag NCs were synthesized by a galvanic replacement reaction. Four mL of Ag nanocube (12 mM in water) were added to 50 mL (1 mg/mL) of aqueous solution of PVP. Different volumes of $HAuCl_4$ (0.24 mM) were added. The product was collected by centrifugation and dispersed in 1 mL of water.

Synthesis of Au−Ag@Au NC. Aqueous suspension (200 μL) of Au−Ag NCs was added to 12.5 mL of aqueous solution containing NaOH, PVP (0.8 mM), and AA (20 mM) under stirring. Next, $HAuCl_4$ solution (0.12 mM) was injected at a rate of 0.02 mL/min. The product was centrifuged and dispersed in water.

FDTD Simulation. Scattering spectra, absorption spectra, and near-field profiles were numerically calculated using FDTD solution. FDTD simulations were performed on a model nanobox (NB) of 60 nm in outer edge length and 5 nm in wall thickness, and on an NC of 60 nm in outer edge length, 6 nm in wall thickness, 12 nm in edge length of hole at the corner, and 4 nm in diameter of hole at the face. The boundary conditions of the computational domain were set to perfectly matched layer-absorbing boundaries. The total simulation volume was equal to 1 μm^3. To confirm the convergence and accuracy, a simulation grid size of 1 nm was used.

Conjugation of PEG with Au−Ag@Au NC. Five mg of mPEG-SH was added to an aqueous suspension of Au−Ag@Au NCs containing 62 μg/mL of Au atoms. Then the solution was incubated overnight in the dark at room temperature. Afterward, the product was washed once with phosphate-buffered saline (PBS) and redispersed in 1 mL of PBS.

Cell Culture and Photothermal Treatment. The MCF-7 breast cancer cell lines were cultured in McCoy's 5a modified medium containing 10% fetal bovine serum (FBS) and 5% streptomycin/penicillin at 37 °C in 5% CO_2 (v/v). The medium was changed 2−3

DOI: 10.1021/acsami.5b08305
ACS Appl. Mater. Interfaces 2015, 7, 21985−21994

times a week. When cells approached a confluency of 80−90%, these cells were harvested and seeded onto a multiwall plate. Cells were cultured in Dulbecco's modified Eagle's medium (DMEM) supplemented with 10% fetal bovine serum and maintained overnight at 37 °C in a humidified 5% CO_2 atmosphere. Then 100 μL of PEGylated Au−Ag@Au NCs (Au−Ag NCs) and the same amount of PBS solution were added into the medium containing 1 mL of culture solution, respectively. The cells were cultured for 3 h. Then cells were irradiated by an 808 nm laser at a power density of 1.0 W/cm^2 for 20 min. Before viability staining, the cells were washed with PBS and were cultured for 5 h at 37 °C in a humidified 5% CO_2 atmosphere. The viability state of the cells was researched by a dark-field microscope.

MTT Assay. The MCF-7 breast cancer cells were seeded in a 96-well microplate in complete DMEM culture medium and were incubated at 37 °C in a humidified atmosphere with 5% CO_2 for 24 h. Next, DMEM solution was removed and fresh DMEM solutions containing different concentrations of PEGylated Au−Ag NCs and Au−Ag@Au NCs were added. The cells were incubated for 12 h at 37 °C with 5% CO_2. Then the wells were washed with PBS for three times and fresh DMEM solution was added. After 20 μL of 3-(4,5-dimethylthiazol-2-yl)-2,5-diphenyltetrazolium bromide (MTT) stock solutions (5 mg/mL) were added to each well, the cells were incubated for another 4 h. To dissolve the produced formazan, 150 μL of dimethyl sulfoxide (DMSO) was added. Absorbance (A) at 490 nm was measured using a microplate reader (ELX 800; BioTek). Cell viabilities were calculated as $A_{experiment}/A_{control} \times 100\%$. A quantitative experiment of photothermal effect was conducted as follows: after being incubated with NCs for 3 h at 37 °C in a humidified 5% CO_2 atmosphere, cells were irradiated with 808 nm laser for 20 min and then incubated for another 12 h. The remaining processes were similar to the described MTT assay.

Measurements. The morphological information on NPs was obtained by transmission electronic microscopy (TEM, JEOL, JEM-2010). Ultraviolet−visible (UV−vis) absorbance spectra were measured by using UV-3600 UV−vis−NI spectrophotometer. High-resolution TEM (HRTEM), energy-dispersive X-ray spectroscopy (EDX) spectrum, line scanning, and elemental mapping were performed using JEM-ARM200F atom resolution analytical microscope, which operated at 200 kV. Cell images were taken using Olympus IX 73 fluorescence microscope.

RESULTS AND DISCUSSION

Permeability of Different Etchants through Traditional SiO_2 Shell. By investigating the morphology and absorption peak of Ag@SiO_2 NPs and Au−Ag NC@SiO_2 incubated with the etchants of Ag element, the permeability of reagent (e.g., NH_4OH, H_2O_2, and $HAuCl_4$) through traditional SiO_2 shell was explored. With the addition of NH_4OH (15 mL, 10 M) and stirring for 2 h, Ag nanocube (62 ± 5 nm)@SiO_2 (10 ± 2 nm) evolved into yolk−shell structure (Figure 1C, E). When 15 mL of H_2O_2 (3 M) was added, Ag core was almost completely etched (the inset in Figure 1E). Obviously, for Ag@SiO_2 NPs, H_2O_2 is a much stronger etchant than NH_4OH. With increasing the thickness of the SiO_2 shell to 60 ± 5 nm, NH_4OH can still easily penetrate through the SiO_2 shell to etch the Ag core (Figure 1F). However, when $HAuCl_4$ was introduced into the aqueous suspension of Ag@SiO_2 (28 ± 3 nm) NPs, the galvanic replacement reaction did not appear. The phenomenon is due to the fact that silica shell prevented $HAuCl_4$ from reacting with the Ag core. Another 5 min later, excess H_2O_2 was injected into the reaction solution to etch the Ag element. Interestingly, the reaction solution suddenly turned red. Seen from Figure 1G, hollow SiO_2 shell structures are produced and there are small Au NPs deposited on the surface of SiO_2 shell. The results indicate that the core is pure Ag and $HAuCl_4$ does not access the inner core before addition of H_2O_2. H_2O_2 plays double roles of etching the inner Ag core and

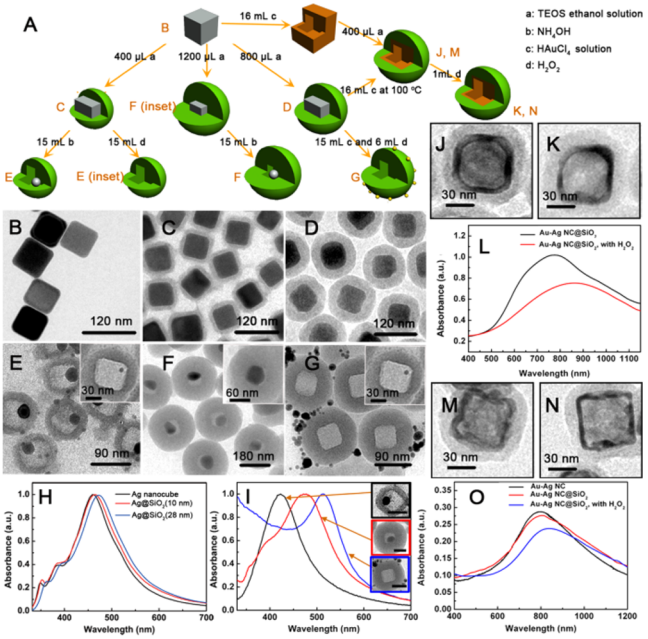

Figure 1. (A) Schematic illustrations and TEM images of (B) Ag NC, (C) Ag NC@SiO_2 (10 ± 2 nm), (D) Ag NC@SiO_2 (28 ± 3 nm), (E) Ag@SiO_2 (10 ± 2 nm) with adding 15 mL of NH_4OH (the inset is obtained by adding 15 mL of H_2O_2), (F) Ag@SiO_2 (60 ± 5 nm) with adding 15 mL of NH_4OH (the inset is the image of Ag@SiO_2 before adding NH_4OH), (G) Ag@SiO_2 (28 ± 3 nm) with adding $HAuCl_4$ and H_2O_2. UV−vis absorbance spectra for NPs (H) corresponding to the TEM images in (B−D) and (I) corresponding to the TEM images in (E−G). Au−Ag NC@SiO_2 synthesized by the reaction of $HAuCl_4$ and Ag nanocube@SiO_2 before (J) and after (K) adding H_2O_2 (5%). (L) UV−vis absorbance spectra corresponding to (J and K). Au−Ag NC@SiO_2 synthesized by coating SiO_2 on the surface of Au−Ag NC before (M) and after (N) adding H_2O_2. (O) UV−vis absorbance spectra corresponding to (M and N). All scale bars are 60 nm in (I).

acting as a reducing agent of $HAuCl_4$, which is due to the fact that the redox potential of H_2O_2 (1.763 V vs SHE at pH < 7; SHE = standard hydrogen electrode) is higher than that of Ag^+/Ag (0.8 V vs SHE) and $AuCl_4^-/Au$ (0.99 V vs SHE).[32,24] As shown in Figure 1H, the absorption peak of Ag nanocube (62 ± 5 nm) shifts monotonically to longer wavelengths with increasing thickness of SiO_2 shell. The dipole resonance peak[34] of the Ag/SiO_2 yolk−shell structure corresponding to Figure 1E is blue-shifted and the quadrupole resonance mode[34] disappears in comparison with the absorption spectrum of Ag nanocube. However, the dipole resonance peak of the Ag/SiO_2 yolk−shell structure corresponding to Figure 1F does not have an obvious shift, which is due to the fact that the red-shifting effect originating from the larger dielectric constant of the surrounding medium offsets the blue-shifting effect resulting from the smaller size. The resonance peak of SiO_2 shell/Au nanospheres (NSs) at 513 nm arises mainly from Au NS on the surface of the SiO_2 shell. Herein, Au−Ag@SiO_2 NCs were synthesized by two methods. The first method involves the reaction of $HAuCl_4$ and the core of Ag@SiO_2 (Figure 1J). Ag@SiO_2 nanocubes were incubated at 100 °C for 30 min before adding $HAuCl_4$ solution. In the second method, Au−Ag NCs were synthesized first and then SiO_2 was deposited on the surface of NC (Figure 1M). After adding 5% aqueous H_2O_2, the LSPR peak intensities of Au−Ag@SiO_2 NPs obtained by the two methods all have a clear decrease together with red-shifting in the peak position (Figure 1L, O). However, the

DOI: 10.1021/acsami.5b08305
ACS Appl. Mater. Interfaces 2015, 7, 21985−21994

LSPR peak intensities of Au−Ag NCs deposited by Au atoms have obvious improvements. After adding 5% aqueous H_2O_2, the SPR peaks of Au−Ag@Au NCs have hardly changed (Figure S5). On the basis of these experimental results, it can be concluded that traditional SiO_2 shell was not an ideal protective layer for improving the chemical stability of NP containing a Ag element.

Morphology and Component of Au−Ag HNP and Au−Ag@Au HNP. Au−Ag HNPs were synthesized by the replacement reaction between Ag and $HAuCl_4$ containing alloying and dealloying processes.[10] Parts A−E of Figure 2 show the TEM images of Au−Ag HNPs obtained by titrating Ag nanocubes with 3, 6, 8, 10, and 12 mL of $HAuCl_4$ (0.24 mM) solution, respectively. These Au−Ag HNPs are unstable in the oxidation environment. When mixed with H_2O_2, the inner Ag content of Au−Ag HNPs shown in Figure 2A was etched, forming Ag-deficient Au−Ag NB structure (Figure 2G). With increasing the amount of H_2O_2, the Ag content in Au−Ag NB would further decrease (Table 1). To stabilize Au−Ag HNP, Au atoms were deposited on the surface of Au−Ag HNP. When $HAuCl_4$ was introduced into the aqueous suspension of Au−Ag HNPs in the presence of AA, Au atoms would be generated through two reactions. Further galvanic replacement reaction (at a rate of R_g) would finally result in Au−Ag HNP fragmentation, whereas the reduction by AA (at a rate of R_r) would result in the deposition of Au atoms on the surface of HNP. The two reactions have a competitive mechanism, which can be controlled by tuning the pH value of the reaction solution and using a slow injection rate for $HAuCl_4$ solution. With the increase of pH, the reduction power of AA can be efficiently improved, whereas the further galvanic replacement reaction was suppressed. When the pH of the reaction solution is increased to 11.02, $R_g \ll R_r$.[31] Significantly, the stronger reduction power of AA in the environment of high pH promotes the rapid reduction of $HAuCl_4$ and achieves galvanic replacement-free deposition of Au atoms on Au−Ag HNP, leading to the reduction of pinhole and increase of shell thickness of Au−Ag HNP (Figure 2F, I, J).

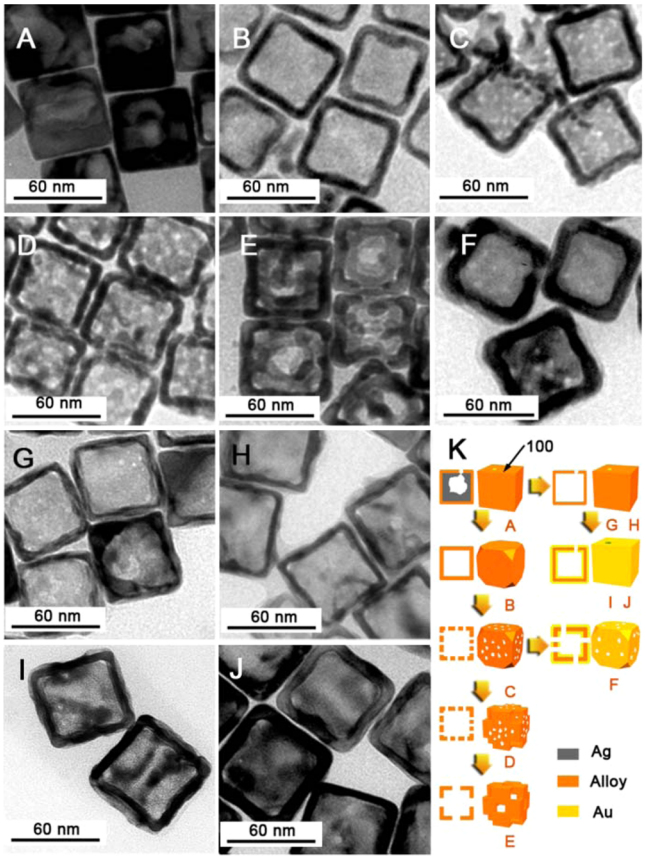

Figure 2. TEM images of Ag nanocubes after reaction with different volumes of 0.24 mM $HAuCl_4$: (A) 3 mL, (B) 6 mL, (C) 8 mL, (D) 10 mL, and (E) 12 mL. (F) TEM image of Au−Ag NCs corresponding to (C) deposited by Au atoms (3.2×10^{-4} mmol). TEM images of Au−Ag NBs shown in (A) with the incubation of (G) 280 μL of H_2O_2, (H) 360 μL of H_2O_2, (I) 280 μL of H_2O_2 and the deposition of Au atoms (1.6×10^{-4} mmol), and (J) 360 μL of H_2O_2 and the deposition of Au atoms (3.2×10^{-4} mmol). (K) Schematic illustrations.

Table 1. Atomic Composition of HNPs Corresponding to Figure 2A, G, H

	weight/%		molar ratio
sample	Au	Ag	Au/Ag
HNPs in Figure 2A	32.66	67.34	0.27
HNPs in Figure 2G	41.93	58.07	0.40
HNPs in Figure 2H	51.50	48.50	0.58

HRTEM images of the Au−Ag NCs and Au−Ag@Au NCs show that the two kinds of nanostructures are single crystalline (Figure 3A, B). Lattice fringes are separated by 0.205 and 0.145 nm, corresponding to {200} and {220} planes of face-centered cubic (fcc) Au/Ag, respectively (gold and silver own the same fcc structure and almost equal lattice constants). On the basis of these observations, it is demonstrated that Au atoms are epitaxially deposited on the surface of Au−Ag HNP. In the growth process of Au−Ag@Au NCs, the factors of thermodynamic and kinetic controls should be taken into account. In the absence or with a relatively low concentration of PVP, the trend typically observed for surface energies of the low-index crystallographic facets in an fcc structure is $\gamma\{111\} < \gamma\{100\} < \gamma\{110\}$.[35] However, in the presence of PVP at a relatively high concentration, the order of $\gamma\{111\}$ and $\gamma\{100\}$ would be reversed because PVP more strongly binds on {100} facets of an fcc structure than {111} facets, resulting in the reduction of $\gamma\{100\}$.[10,35] In our case, after depositing Au atoms, the pinhole on the {100} facet of Au−Ag NC would disappear or be reduced. Au atoms are deposited along the fringe of the pinhole on the {100} facet, which results in the enlargement of the {100} facet. As the growth proceeds, the concentration of PVP in the reaction solution would drop and the deposition of Au atoms would preferentially takes place on the high-energy {100} facet of Au−Ag NC, resulting in the increase of shell thickness in Au−Ag NC (Figure 3C, E, G, I). From the line profiles of EDX, it is clearly found that the element distribution trend of Au and Ag is consistent in Au−Ag NC, whereas the Au atoms dominate in the outer and inner surfaces of Au−Ag@Au NC (Figure 3K, L).

Stability Studies of Au−Ag HNP and Au−Ag@Au HNP. The stabilities of Au−Ag NCs and Au−Ag@Au NCs were monitored by UV−vis spectra. The SPR peak of Au−Ag NCs would be red-shifted from 589 to 977 nm with increasing $HAuCl_4$ amount (Figure 4A). When 280 μL of H_2O_2 was added, the SPR peak of Au−Ag HNPs at 589 nm was red-shifted to 712 nm. With the deposition of Au atoms, the LSPR peak position of Ag-deficient Au−Ag@Au NCs was further blue-shifted to 673 nm, together with an increase in extinction peak intensity and narrowing in the full width at half-maximum

DOI: 10.1021/acsami.5b08305
ACS Appl. Mater. Interfaces 2015, 7, 21985−21994

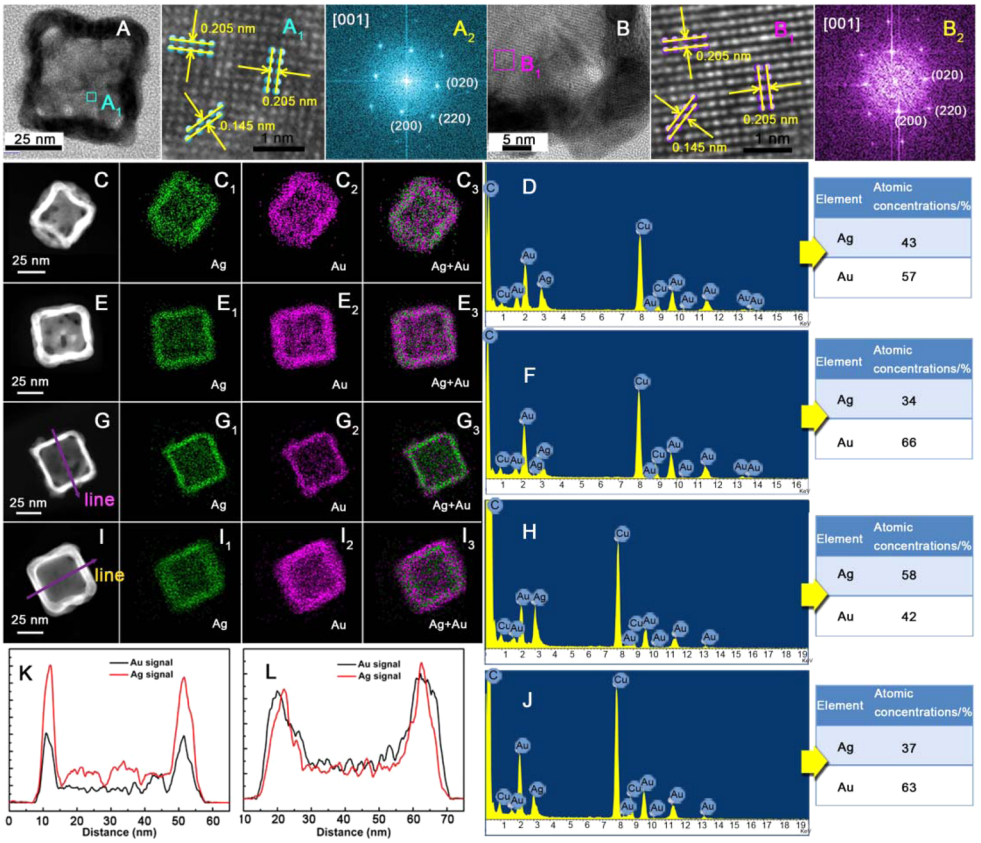

Figure 3. (A, A_1) HRTEM images of Au−Ag NC, (A_2) corresponding fast Fourier-transformed (FFT) patterns; (B, B_1) HRTEM images of Au−Ag@Au NC, (B_2) corresponding FFT patterns. Dark-field scanning transmission electron microscopy (DF-STEM) images and EDX elemental mapping of Au−Ag NC obtained by adding 10 mL of $HAuCl_4$ (C) before and (E) after the deposition of Au atoms, Au−Ag NC obtained by adding 6 mL of $HAuCl_4$ (G) before and (I) after the deposition of Au atoms. (D, F, H, J) EDX spectra of NPs and the atomic concentrations of Au and Ag corresponding to (C, E, G, I). EDX line profiles of (K) Au−Ag NC corresponding to the image in (G), (L) Au−Ag@Au NC corresponding to (I).

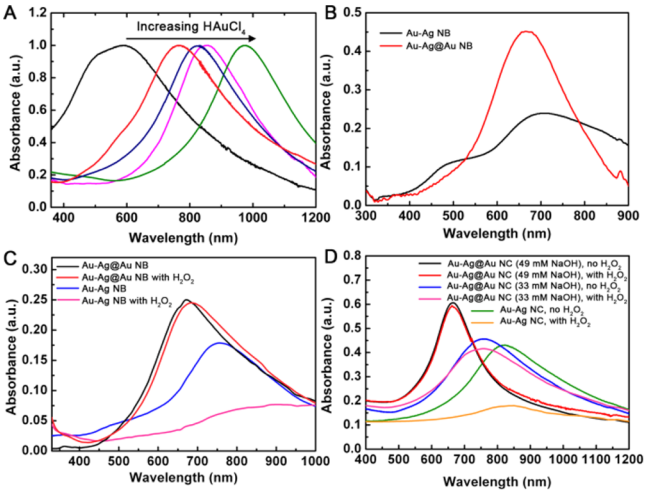

Figure 4. UV−vis absorbance spectra of (A) Au−Ag HNPs obtained by adding different volumes (3, 6, 8, 10, and 12 mL) of 0.24 mM aqueous $HAuCl_4$; (B) Au−Ag NBs and Au−Ag@Au NBs corresponding to Figure 2 G, I; (C) Au−Ag NBs and Au−Ag@Au NBs corresponding to Figure 2 H, J before and after mixing with 5% aqueous H_2O_2 for 6 h. (D) Comparison of chemical stabilities in H_2O_2 environment for Au−Ag NCs and Au−Ag@Au NCs synthesized with different concentrations of NaOH.

(fwhm) (Figure 4B). The scattering effect of the Au−Ag boundary on the conduction electrons will contribute to the broadening of the extinction spectrum, which leads to damping of the surface plasmons.[29] The introduction of Au atoms makes the Au element predominant and decreases the scattering effect. Au shell would not cause a significant change of the dielectric constant. While the increase of the size for NPs would induce the red-shifting effect, the blue-shift from 712 to 673 nm was mainly attributed to the increase of wall thickness and change of morphology. With adding more H_2O_2 (360 μL), the LSPR peak of Au−Ag HNPs was red-shifted to 757 nm. As anticipated, the LSPR peak of Au−Ag HNPs can also be tuned to 673 nm by increasing the Au atoms deposited on the surface of HNP. Upon mixing with excess H_2O_2 for 6 h, the extinction peak of Ag-deficient Au−Ag NBs appeared a very large red-shift and the intensity greatly decreased. However, the LSPR peak of Ag-deficient Au−Ag@Au NBs had only a red-shift of ∼5 nm, while the peak intensity had almost no change (Figure 4C). In addition, a set of experiments were performed to investigate the influence of NaOH concentration on the LSPR peak position of obtained Au−Ag@Au NCs. When NaOH concentration was adjusted from 33 to 49 mM while keeping the other reaction parameters unaltered, it was found that the LSPR peak of Au−Ag NCs was blue-shifted from 820 to 760 nm and 665 nm, respectively (Figure 4D). With the increase of NaOH concentration, Au−Ag@Au NCs show a large blue-shift, together with obvious narrowing in fwhm (Figure S6), which indicates that the increase of pH can effectively improve the reaction power of AA. As shown in Figure 4D, the Au−Ag@Au NC structures obtained in different concentrations of NaOH

DOI: 10.1021/acsami.5b08305
ACS Appl. Mater. Interfaces 2015, 7, 21985−21994

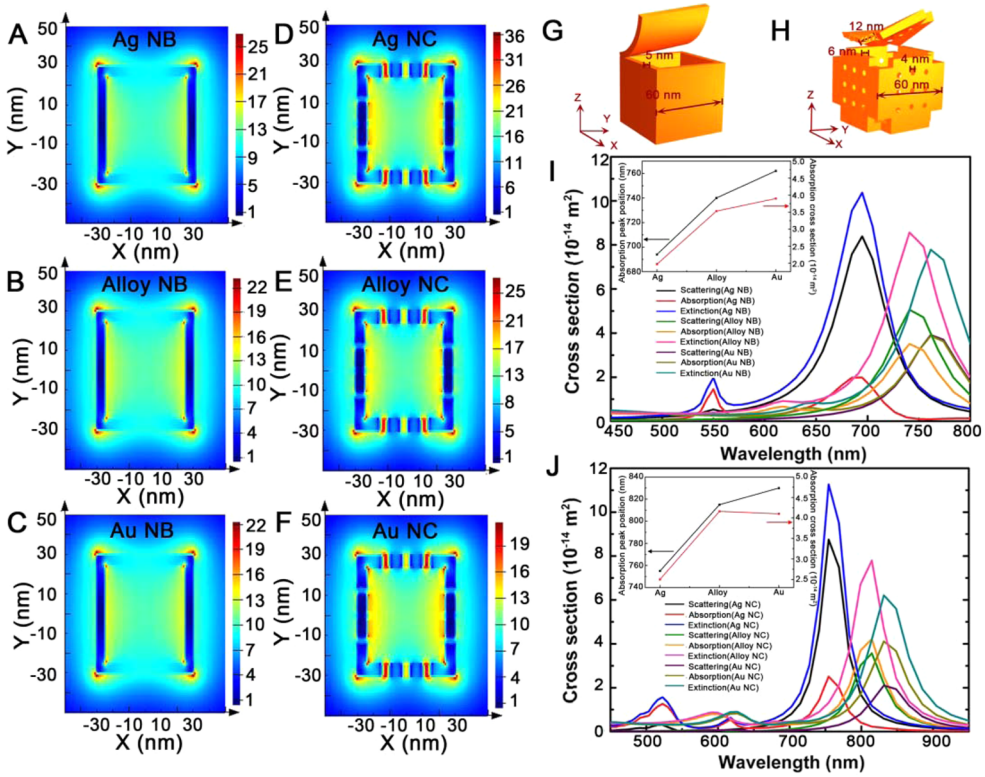

Figure 5. Electric field distribution of (A) Ag NB, (B) alloy NB (Au/Ag ratio = 2), (C) Au NB, (D) Ag NC, (E) alloy NC (Au/Ag ratio = 2), and (F) Au NC. (G) NB and (H) NC template used for the simulations. Calculated absorption, scattering, extinction cross section of (I) NB (inset is the summary of the dependence of absorption peak position and absorption cross section on the component of NB) and (J) NC (inset is the summary of the dependence of absorption peak position and absorption cross section on the component of NC) in water solution.

solution show strong chemical stability with the incubation of aqueous H_2O_2 for 6 h. Collectively, the SPR peak position of Au−Ag@Au HNPs can be manipulated by controlling the amount of $HAuCl_4$ and NaOH added into the reaction solution, while the chemical stability of Au−Ag@Au HNPs in oxidative environment has significant improvement compared with Au−Ag HNPs.

FDTD Simulation for the Optical Properties of HNP. To gain insights into the optical properties of Au−Ag HNPs (including NB and NC), further FDTD calculation was conducted to research the local electric field distribution and spectra (absorption, scattering, and extinction) of these NPs. A linearly polarized plane wave irradiates NP along the *z*-axis. The field profiles perpendicular to incidence direction were calculated at SPR resonant mode. Of note, the electric field intensities of HNPs are located mainly at the position with a small radius of curvature, such as corners and pinholes (Figure 5A−F). The extinction cross section is obtained by the equation $C_{ext} = C_{scat} + C_{abs}$ (where C_{abs} is the absorption cross section and C_{scat} is the scattering cross section).[16] The experimental results and the FDTD calculations show that the extinction peak of NC was red-shifted compared with NB, while the SPR peak position of HNPs was monotonously blue-shifted with increasing the ratio of Ag/Au (Figure 5I, J). Intraband absorption of Au and Ag determines the LSPR properties of the alloy for UV to 500 nm.[5,36] However, for region 600 nm to NIR, interband transition is negligible, and the Drude equation can be used.[36] The real part of relative permittivity ε_1 is a dominant parameter for the observed LSPR spectral shift in the experiment.[36,37] Therefore, the Drude equation would well explain the red-shift of scattering and absorption peak of HNPs with the increase of Au content (Figure S10). Seen from Figure 5I, the ratio of C_{abs}/C_{ext} for NB increases from 18.8% to 41.5% to 50.0% with improving the Au content of NB from pure Ag, to alloy (the ratio of Au/Ag = 2), to pure Au. Similarly, the absorption cross section C_{abs} of Au NC corresponds to 66.1% of the total extinction cross section C_{ext} and the ratio of C_{abs}/C_{ext} for alloy NC is 54.0%, whereas the C_{abs} of pure Ag only contributes to 22.2% of C_{ext} (Figure 5J). In addition, it was found that the absorption cross section of alloy NC is almost equivalent to that of pure Au NC. With the deposition of Au atoms, the plasmonic property of Au−Ag HNPs is dominated by Au. The larger absorption cross section and the smaller scattering cross section of Au would endow the obtained Au−Ag@Au NCs with higher photothermal efficiency.

Photothermal Transduction Efficiencies. The photothermal transduction efficiencies clearly demonstrate the ability of NPs converting absorbed light energy into thermal energy. Inspired by the FDTD calculated results, the correlation between the photothermal transduction efficiencies and the Au/Ag composition ratio of HNPs was investigated experimentally. The SPR peak positions of Au−Ag@Au NCs and Au−Ag NCs counterparts were tuned to the NIR region. The Au/Ag molar ratio in Au−Ag NC was 1.29. After depositing Au atoms, the Au/Ag molar ratio increased to 1.76. Therefore, the molar ratio of Au/Ag/Au in Au−Ag@Au NC was concluded to be 1.29/1/0.47 (Table 2). For the purpose of comparison, the extinction intensities of Au−Ag NCs and Au−Ag@Au NCs were adjusted to be the same at 808 nm (Figure 6A). The temperature changes were measured as a function of time under the irradiation of 808 nm laser at a power density of 1

DOI: 10.1021/acsami.5b08305
ACS Appl. Mater. Interfaces 2015, 7, 21985−21994

Table 2. Atomic Composition of Au−Ag and Au−Ag@Au NCs in Photothermal Therapy

	weight/%		molar ratio
sample	Au	Ag	Au/Ag
Au−Ag NCs	70.34	29.66	1.29
Au−Ag@Au NCs	76.28	23.72	1.76

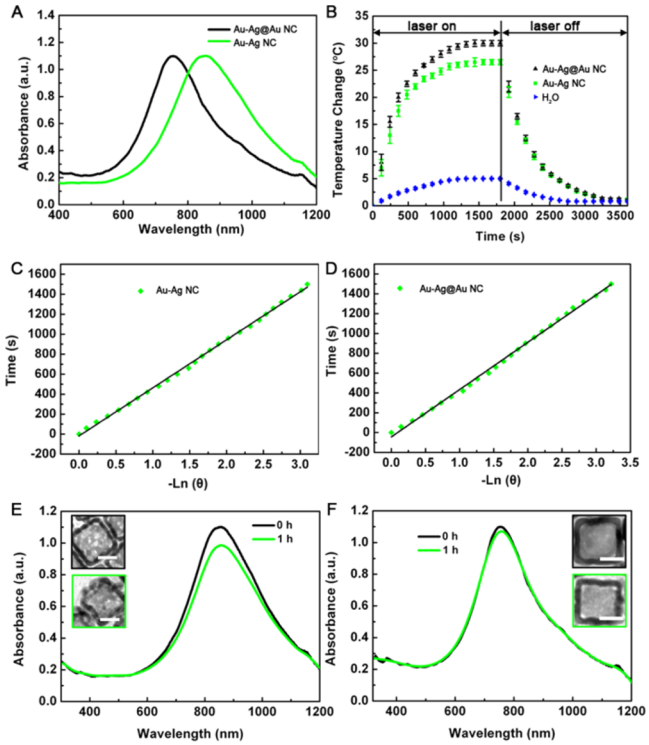

Figure 6. (A) UV−vis absorbance spectra of Au−Ag NCs and Au−Ag@Au NCs dispersed in deionized water. (B) Temperature change in the solution for Au−Ag NCs, Au−Ag@Au NCs, and water irradiated by NIR laser (808 nm, 1 W/cm^2), in which the irradiation lasted for 30 min and then the laser was shut off. The volume of solution is 2 mL. (C, D) Time constants for heat transfer from the system containing Au−Ag NCs and Au−Ag@Au NCs were calculated to be τ_{s1} = 480.73 s and τ_{s2} = 477.30 s by applying the linear time data from the cooling period versus negative natural logarithm of driving force temperature, respectively. UV−vis absorbance spectra of (E) Au−Ag NCs and (F) Au−Ag@Au NCs before (black line) and after (green line) irradiation. (The insets are TEM images before and after laser irradiation.) All the bars are 30 nm.

W/cm^2 (Figure 6B). After reaching equilibrium, the system was cooled to ambient temperature. The process is described in the following energy-balance equation,

$$\sum_i m_i C_{p,i} \frac{dT}{dt} = Q_1 + Q_0 - Q_{amb} \quad (1)$$

where m_i and $C_{p,i}$ are the mass and heat capacity of each component of the sample cell, T is the sample cell temperature, Q_1 is the energy inputted by NPs, Q_0 is the heat energy inputted by the sample cell and solvent without NPs, and Q_{amb} is the outgoing energy.

The correlation of temperature and the outgoing thermal energy is shown as follows,

$$Q_{amb} = hS(T - T_{amb}) \quad (2)$$

where h is the heat transfer coefficient, S is the sample well surface area, and T_{amb} is the ambient room temperature.

The thermal time constant can be presented as follows:

$$\tau = \frac{\sum_i m_i C_{p,i}}{hS} \quad (3)$$

Equations 2 and 3 were substituted into eq 1 and rearranged to yield

$$hS\tau \frac{dT}{dt} = Q_1 + Q_0 - hs(T - T_{amb}) \quad (4)$$

To simplify the calculation process, the variable θ was introduced:[38]

$$\theta = \frac{T - T_{amb}}{T_{max} - T_{amb}} \quad (5)$$

where T_{max} is the steady-state maximum temperature.

During the cooling process, the laser source was shut off. Rearranging and integrating the equation[38] provides the following expression:

$$t = -\tau \ln \theta \quad (6)$$

Clearly, once the thermal time constant τ is obtained, the heat transfer coefficient h can be easily calculated.

When the system temperature rises to a maximum, the power flowing into the sample cell is equivalent to the power outflowing:

$$Q_1 + Q_0 = hS(T_{max} - T_{amb}) \quad (7)$$

According to the report by Roper et al.,[39] the photothermal conversion efficiency can be measured using the follow equation,

$$\eta = \frac{hS(T_{max} - T_{amb}) - Q_0}{I(1 - 10^{-A})} \quad (8)$$

where I is the incident laser power and A is the absorbance of Au NP at 808 nm. The heat energy Q_0 was measured to be 75.5 mW independently. Seen from Figure 6B, the photothermal responses of Au−Ag NCs increased the solution temperature by 26.5 °C and those of Au−Ag@Au NCs increased by 30 °C after exposure to laser for 30 min. In the absence of NPs, the solution increased by only 5 °C under the same irradiation condition. According to the data obtained from Figure 6, the photothermal transduction efficiency η of Au−Ag NCs was calculated by eq 8 to be 31.2%. Compared with Au−Ag NCs, the photothermal transduction efficiency of Au−Ag@Au NCs (36.5%) is higher, which should be attributed to the higher Au content in Au−Ag@Au NC. To further confirm this viewpoint, Ag-deficient Au−Ag@Au NCs were synthesized by etching Au−Ag NCs with 300 μL of H_2O_2 and depositing 1.6 × 10^{-4} mmol of Au atoms. As expected, the photothermal transduction efficiency of Ag-deficient Au−Ag@Au NCs (37.9%) is noticeably higher than that for the corresponding Au−Ag NCs (30%) (Figure S11). For Ag-deficient Au−Ag NCs, the etching of the Ag element would result in a dramatic reduction and red-shift of the SPR peak, which would cause a significant reduction of the molar extinction coefficient. To optimize the molar extinction coefficient and photothermal transduction efficiencies simultaneously, Au−Ag@Au NCs were considered to be more excellent photothermal agents than Ag-deficient Au−Ag@Au NCs. In addition, the absorption intensity of Au−Ag NCs under laser irradiation for 1 h has a slight decrease

DOI: 10.1021/acsami.5b08305
ACS Appl. Mater. Interfaces 2015, 7, 21985−21994

(Figure 6E), while the absorption peak intensity of Au−Ag@Au NCs remains the same, which indicates that Au−Ag@Au NCs were able to maintain the photothermal conversion efficiency during photothermal therapy (Figure 6F).

MTT and Photothermal Therapy. To demonstrate the application of Au−Ag@Au NC, the MCF-7 breast cancer cells were assigned to four groups: (1) control group one treated with phosphate-buffered saline (PBS) and without laser irradiation; (2) control group two treated with PBS and laser irradiation for 20 min; (3) control group three treated with NC structures (19.5 μg/mL) and without laser irradiation; and (4) the experimental group treated with NC structures (19.5 μg/mL) plus laser irradiation for 20 min. After being cultured for 5 h, the cells were stained by fluorescent terminating agent (containing metanil yellow and ethidium bromide) to assess the viability. Metanil yellow reacted with cell membrane and dyed the membrane of live cells green. Ethidium bromide penetrated through the damaged cell membrane, turning the cell nucleus orange−red. Therefore, orange−red-stained cells are dead cells, and green-stained cells are live cells. Moderate cell hyperthermia occurs at 43 °C, which causes an increase in endocytosis, uptake of drugs, and blood flow and a breakdown in cellular structure.[40] When temperature is increased over 46 °C, severe hyperthermia and eventual cell death appear through heat ablation.[40,41] Control group two shows that exposure of the cells to the NIR laser in the absence of composite structures did not compromise cell viability. The phenomenon reveals that the irradiation intensity of NIR laser has hardly any influence on the viability of cells (Figure 7B). The cell viability assay in control group three did not exhibit clear cell death, which demonstrates that Au−Ag@Au NCs show no sign of cytotoxicity up to 5 h (Figure 7C). Significant cellular breakdown and necrosis phenomena were observed in the experimental group, which indicates that the localized temperature on the surface of the cells should be >46 °C (Figure 7D). In quantitative analysis, the cell viabilities of MCF-7 breast cancer cells incubated with NCs of different concentrations ranging from 4.5 to 70 μg/mL show less toxicity (Figure 7E). The PEGylated Au−Ag@Au NCs show slightly higher cell viability compared with PEGylated Au−Ag NCs at the same weight concentration, which is possibly due to the low concentration of the Ag element. After irradiation for 20 min, the cell viabilities of MCF-7 breast cancer cells incubated with PEGylated Au−Ag NCs and PEGylated Au−Ag@Au NCs show a clear reduction (Figure 7F). The sample treated with PEGylated Au−Ag@Au NCs shows higher cell death (97%) than PEGylated Au−Ag NCs (73%). The experimental results prove that the photothermal effect of Au−Ag NCs was greatly improved by depositing Au atoms.

CONCLUSIONS

By researching the permeability of NH_4OH and H_2O_2 through SiO_2 shell, it was found that the SiO_2 shell cannot protect Au−Ag NCs in an oxidation environment. Herein, Au atoms were deposited on the surface of Au−Ag NC to generate Au−Ag@Au NC by improving the reduction power of AA at a sufficiently high solution pH. It was found that the obtained Au−Ag@Au NCs embraced much stronger extinction peaks, narrower bandwidths, and higher chemical stabilities compared with Au−Ag NCs. FDTD calculation results suggest that the contribution of absorption to extinction cross section would increase with improving the ratio of Au/Ag. Moreover, the photothermal transduction efficiency of Au−Ag@Au NCs

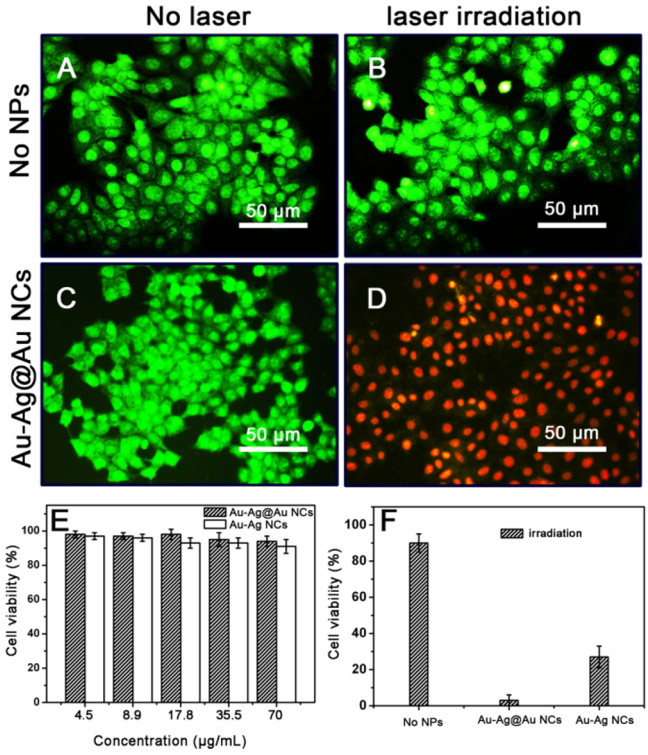

Figure 7. Comparison of photothermal destruction of MCF-7 breast cancer cells without (A, B) and with (C, D) the incubation of PEGylated Au−Ag@Au NCs. Cell irradiated by 808 nm diode laser at power densities of 1 W/cm^2. (E) Cell viability of MCF-7 breast cancer cells after incubation with different concentrations of PEGylated Au−Ag NCs and PEGylated Au−Ag@Au NCs. (F) Viability of cells incubated with PBS, PEGylated Au−Ag@Au NCs, and PEGylated Au−Ag NCs after irradiation.

(36.5%) was higher than that of Au−Ag NCs (31.2%), which is consistent with the FDTD calculation result. Under the resonance excitation of NIR laser, PEGylated Au−Ag@Au NCs were activated to cause hyperthermia, leading to significant MCF-7 breast cancer cells death. Au−Ag@Au NC structures with improved photothermal efficiency and enhanced chemical stability can be further studied and have a planned in vivo trial application.

ASSOCIATED CONTENT

Supporting Information

The Supporting Information is available free of charge on the ACS Publications website at DOI: 10.1021/acsami.5b08305.

TEM images of Ag nanocube@SiO_2 incubated with NH_4OH; absorption spectra of Ag nanocubes with different reaction times; the histogram of the size distribution of Ag nanocubes; the thickness distribution of SiO_2 shell; summarization of peak position and full width at half-maximum of Au−Ag and Au−Ag@Au HNPs; absorption spectra of Au−Ag@Au NCs synthesized with different concentrations of PVP and different injection rates; real part and imaginary part of the refractive index of Au and Ag; the permittivity of Au, Ag, and alloy; absorption spectra of Au−Ag NC and Ag-deficient Au−Ag@Au NCs dispersed in deionized water and corresponding temperature change; the fluorescence image of cells incubated with Au−Ag NCs (PDF)

DOI: 10.1021/acsami.5b08305
ACS Appl. Mater. Interfaces 2015, 7, 21985−21994

AUTHOR INFORMATION

Corresponding Authors

*E-mail: xrx2041@163.com.
*E-mail: lx-zhu@163.com.
*E-mail: xlxu@ustc.edu.cn.

Notes

The authors declare no competing financial interest.

ACKNOWLEDGMENTS

This work was supported by the National Natural Science Foundation of China (no. 51272246 and no. 81172082).

REFERENCES

(1) Pelaz, B.; Grazu, V.; Ibarra, A.; Magen, C.; Del Pino, P.; De la Fuente, J. M. Tailoring the Synthesis and Heating Ability of Gold Nanoprisms for Bioapplications. *Langmuir* **2012**, *28* (24), 8965−8970.

(2) Yang, Y.; Zhang, Q.; Fu, Z. W.; Qin, D. Transformation of Ag Nanocubes into Ag−Au Hollow Nanostructures with Enriched Ag Contents to Improve SERS Activity and Chemical Stability. *ACS Appl. Mater. Interfaces* **2014**, *6* (5), 3750−3757.

(3) Ng, V. W. K.; Berti, R.; Lesage, F.; Kakkar, A. Gold: A Versatile Tool for In Vivo Imaging. *J. Mater. Chem. B* **2013**, *1*, 9−25.

(4) Kong, X.; Yu, Q.; Zhang, X.; Du, X.; Gong, H.; Jiang, H. Synthesis and Application of Surface Enhanced Raman Scattering (SERS) Tags of Ag@SiO_2 Core/Shell Nanoparticles in Protein Detection. *J. Mater. Chem.* **2012**, *22*, 7767−7774.

(5) Jang, H.; Min, D. Spherically-Clustered Porous Au−Ag Alloy Nanoparticle Prepared by Partial Inhibition of Galvanic Replacement and Its Application for Efficient Multimodal Therapy. *ACS Nano* **2015**, *9*, 2696−2703.

(6) Li, J.; Han, J.; Xu, T.; Guo, C.; Bu, X.; Zhang, H.; Wang, L.; Sun, H.; Yang, B. Coating Urchinlike Gold Nanoparticles with Polypyrrole Thin Shells To Produce Photothermal Agents with High Stability and Photothermal Transduction Efficiency. *Langmuir* **2013**, *29*, 7102−7110.

(7) Maestro, L. M.; Haro-Gonzalez, P.; Sanchez-Iglesias, A.; Liz-Marzan, L. M.; Garcia Sole, J.; Jaque, D. Quantum Dot Thermometry Evaluation of Geometry Dependent Heating Efficiency in Gold Nanoparticles. *Langmuir* **2014**, *30* (6), 1650−1658.

(8) Ayala-Orozco, C.; Urban, C.; Knight, M. W.; Urban, A. S.; Neumann, O.; Bishnoi, S. W.; Mukherjee, S.; Goodman, A. M.; Charron, H.; Mitchell, T.; Shea, M.; Roy, R.; Nanda, S.; Schiff, R.; Halas, N. J.; Joshi, A. Au Nanomatryoshkas As Efficient Near-Infrared Photothermal Transducers for Cancer Treatment: Benchmarking against Nanoshells. *ACS Nano* **2014**, *8*, 6372−6381.

(9) Yang, L.; Tseng, Y.-T.; Suo, G.; Chen, L.; Yu, J.; Chiu, W.-J.; Huang, C.-C.; Lin, C.-H. Photothermal Therapeutic Response of Cancer Cells to Aptamer−Gold Nanoparticle-Hybridized Graphene Oxide under NIR Illumination. *ACS Appl. Mater. Interfaces* **2015**, *7*, 5097−5106.

(10) Chen, J.; McLellan, J. M.; Siekkinen, A.; Xiong, Y.; Li, Z.-Y.; Xia, Y. Facile Synthesis of Gold−Silver Nanocages with Controllable Pores on the Surface. *J. Am. Chem. Soc.* **2006**, *128*, 14776−14777.

(11) Jang, L.-W.; Jeon, D.-W.; Sahoo, T.; Polyakov, A. Y.; Saravanakumar, B.; Yu, Y.-T.; Cho, Y.-H.; Yang, J.-K.; Lee, I.-H. Energy Coupling Processes in InGaN/GaN Nanopillar Light Emitting Diodes Embedded with Ag and Ag/SiO_2 Nanoparticles. *J. Mater. Chem.* **2012**, *22*, 21749−21753.

(12) Rycenga, M.; Cobley, C. M.; Zeng, J.; Li, W.; Moran, C. H.; Zhang, Q.; Qin, D.; Xia, Y. Controlling the Synthesis and Assembly of Silver Nanostructures for Plasmonic Applications. *Chem. Rev.* **2011**, *111* (6), 3669−3712.

(13) Mieszawska, A. J.; Mulder, W. J. M.; Fayad, Z. A.; Cormode, D. P. Multifunctional Gold Nanoparticles for Diagnosis and Therapy of Disease. *Mol. Pharmaceutics* **2013**, *10*, 831−847.

(14) Zuloaga, J.; Nordlander, P. On the Energy Shift between Near-field and Far-field Peak Intensities in Localized Plasmon Systems. *Nano Lett.* **2011**, *11* (3), 1280−1283.

(15) Deeb, C.; Zhou, X.; Miller, R.; Gray, S. K.; Marguet, S.; Plain, J.; Wiederrecht, G. P.; Bachelot, R. Mapping the Electromagnetic Near-Field Enhancements of Gold Nanocubes. *J. Phys. Chem. C* **2012**, *116* (46), 24734−24740.

(16) Mahmoud, M. A.; Chamanzar, M.; Adibi, A.; El-Sayed, M. A. Effect of the Dielectric Constant of the Surrounding Medium and the Substrate on the Surface Plasmon Resonance Spectrum and Sensitivity Factors of Highly Symmetric Systems: Silver Nanocubes. *J. Am. Chem. Soc.* **2012**, *134* (14), 6434−6442.

(17) Park, K.; Biswas, S.; Kanel, S.; Nepal, D.; Vaia, R. A. Engineering the Optical Properties of Gold Nanorods: Independent Tuning of Surface Plasmon Energy, Extinction Coefficient, and Scattering Cross Section. *J. Phys. Chem. C* **2014**, *118* (11), 5918−5926.

(18) Wang, Y.; Black, K. C. L.; Luehmann, H.; Li, W.; Zhang, Y.; Cai, X.; Wan, D.; Liu, S.-Y.; Li, M.; Kim, P.; Li, Z.-Y.; Wang, L. V.; Liu, Y.; Xia, Y. Comparison Study of Gold Nanohexapods, Nanorods, and Nanocages for Photothermal Cancer Treatment. *ACS Nano* **2013**, *7* (3), 2068−2077.

(19) Wang, S.; Riedinger, A.; Li, H.; Fu, C.; Liu, H.; Li, L.; Liu, T.; Tan, L.; Barthel, M. J.; Pugliese, G.; De Donato, F.; D'Abbusco, M. S.; Meng, X.; Manna, L.; Meng, H.; Pellegrino, T. Plasmonic Copper Sulfide Nanocrystals Exhibiting Near-Infrared Photothermal and Photodynamic Therapeutic Effects. *ACS Nano* **2015**, *9*, 1788−1800.

(20) Skrabalak, S. E.; Chen, J.; Sun, Y.; Lu, X.; Au, L.; Cobley, C. M.; Xia, Y. Gold Nanocages: Synthesis, Properties, and Applications. *Acc. Chem. Res.* **2008**, *41* (12), 1587−1595.

(21) Tian, L.; Gandra, N.; Singamaneni, S. Monitoring Controlled Release of Payload from Gold Nanocages Using Surface Enhanced Raman Scattering. *ACS Nano* **2013**, *7*, 4252−4260.

(22) Skrabalak, S. E.; Au, L.; Li, X.; Xia, Y. Facile Synthesis of Ag Nanocubes and Au Nanocages. *Nat. Protoc.* **2007**, *2* (9), 2182−2190.

(23) Goodman, A. M.; Cao, Y.; Urban, C.; Neumann, O.; Ayala-Orozco, C.; Knight, M. W.; Joshi, A.; Nordlander, P.; Halas, N. J. The Surprising In Vivo Instability of Near-IR-Absorbing Hollow Au−Ag Nanoshells. *ACS Nano* **2014**, *8*, 3222−3231.

(24) Zhang, Q.; Cobley, C. M.; Zeng, J.; Wen, L. P.; Chen, J.; Xia, Y. Dissolving Ag from Au−Ag Alloy Nanoboxes with H_2O_2: A Method for Both Tailoring the Optical Properties and Measuring the H_2O_2 Concentration. *J. Phys. Chem. C* **2010**, *114* (14), 6396−6400.

(25) Liu, Z.; Cheng, L.; Zhang, L.; Yang, Z.; Liu, Z.; Fang, J. Sub-100 nm Hollow Au−Ag Alloy Urchin-Shaped Nanostructure with Ultrahigh Density of Nanotips for Photothermal Cancer Therapy. *Biomaterials* **2014**, *35*, 4099−4107.

(26) Khlebtsov, B.; Panfilova, E.; Khanadeev, V.; Bibikova, O.; Terentyuk, G.; Ivanov, A.; Rumyantseva, V.; Shilov, I.; Ryabova, A.; Loshchenov, V.; Khlebtsov, N. G. Nanocomposites Containing Silica Coated Gold−Silver Nanocages and Yb-2,4-Dimethoxyhematoporphyrin: Multifunctional Capability of IR-Luminescence Detection, Photosensitization, and Photothermolysis. *ACS Nano* **2011**, *5*, 7077−7089.

(27) Li, C.-H.; Jamison, A. C.; Rittikulsittichai, S.; Lee, T.-C.; Lee, T. R. In Situ Growth of Hollow Gold−Silver Nanoshells within Porous Silica Offers Tunable Plasmonic Extinctions and Enhanced Colloidal Stability. *ACS Appl. Mater. Interfaces* **2014**, *6*, 19943−19950.

(28) Bai, Z.; Chen, R.; Si, P.; Huang, Y.; Sun, H.; Kim, D. H. Fluorescent PH Sensor Based on Ag@SiO_2 Core−Shell Nanoparticle. *ACS Appl. Mater. Interfaces* **2013**, *5* (12), 5856−5860.

(29) Gao, C.; Hu, Y.; Wang, M.; Chi, M.; Yin, Y. Fully Alloyed Ag/Au Nanospheres: Combining the Plasmonic Property of Ag with the Stability of Au. *J. Am. Chem. Soc.* **2014**, *136*, 7474−7479.

(30) Shahjamali, M. M.; Bosman, M.; Cao, S.; Huang, X.; Saadat, S.; Martinsson, E.; Aili, D.; Tay, Y. Y.; Liedberg, B.; Loo, S. C. J.; Zhang, H.; Boey, F.; Xue, C. Gold Coating of Silver Nanoprisms. *Adv. Funct. Mater.* **2012**, *22* (4), 849−854.

(31) Yang, Y.; Liu, J.; Fu, Z. W.; Qin, D. Galvanic Replacement-Free Deposition of Au on Ag for Core−Shell Nanocubes with Enhanced

DOI: 10.1021/acsami.5b08305
ACS Appl. Mater. Interfaces 2015, 7, 21985−21994

Chemical Stability and SERS Activity. *J. Am. Chem. Soc.* **2014**, *136* (23), 8153−8156.
(32) Murshid, N.; Gourevich, I.; Coombs, N.; Kitaev, V. Gold Plating of Silver Nanoparticles for Superior Stability and Preserved Plasmonic and Sensing Properties. *Chem. Commun.* **2013**, *49*, 11355−11357.
(33) Zhang, Q.; Li, W.; Wen, L.-P.; Chen, J.; Xia, Y. Facile Synthesis of Ag Nanocubes of 30 to 70 nm in Edge Length with CF_3COOAg as a Precursor. *Chem.—Eur. J.* **2010**, *16*, 10234−10239.
(34) Zhou, F.; Li, Z.-Y.; Liu, Y.; Xia, Y. Quantitative Analysis of Dipole and Quadrupole Excitation in the Surface Plasmon Resonance of Metal Nanoparticles. *J. Phys. Chem. C* **2008**, *112*, 20233−20240.
(35) Xia, X.; Xia, Y. Symmetry Breaking during Seeded Growth of Nanocrystals. *Nano Lett.* **2012**, *12*, 6038−6042.
(36) Nishijima, Y.; Akiyama, S. Unusual Optical Properties of the Au/Ag Alloy at the Matching Mole Fraction. *Opt. Mater. Express* **2012**, *2*, 1226−1235.
(37) Liaw, J.-W.; Cheng, J.-C.; Ma, C.; Zhang, R. Theoretical Analysis of Plasmon Modes of Au−Ag Nanocages. *J. Phys. Chem. C* **2013**, *117*, 19586−19592.
(38) Tian, Q.; Jiang, F.; Zou, R.; Liu, Q.; Chen, Z.; Zhu, M.; Yang, S.; Wang, J.; Wang, J.; Hu, J. Hydrophilic Cu_9S_5 Nanocrystals: A Photothermal Agent with a 25.7% Heat Conversion Efficiency for Photothermal Ablation of Cancer Cells In Vivo. *ACS Nano* **2011**, *5*, 9761−9771.
(39) Roper, D. K.; Ahn, W.; Hoepfner, M. Microscale Heat Transfer Transduced by Surface Plasmon Resonant Gold Nanoparticles. *J. Phys. Chem. C* **2007**, *111*, 3636−3641.
(40) Hessel, C. M.; Pattani, V. P.; Rasch, M.; Panthani, M. G.; Koo, B.; Tunnell, J. W.; Korgel, B. A. Copper Selenide Nanocrystals for Photothermal Therapy. *Nano Lett.* **2011**, *11*, 2560−2566.
(41) Peralta, D. V.; Heidari, Z.; Dash, S.; Tarr, M. A. Hybrid Paclitaxel and Gold Nanorod-Loaded Human Serum Albumin Nanoparticles for Simultaneous Chemotherapeutic and Photothermal Therapy on 4T1 Breast Cancer Cells. *ACS Appl. Mater. Interfaces* **2015**, *7*, 7101−7111.

DOI: 10.1021/acsami.5b08305
ACS Appl. Mater. Interfaces 2015, 7, 21985−21994